

3D-MASNet: 3D Mixed-scale Asymmetric Convolutional Segmentation Network for 6-month-old Infant Brain MR Images

Zilong Zeng^{1,2,3}, Tengda Zhao^{1,2,3*}, Lianglong Sun^{1,2,3}, Yihe Zhang^{1,2,3}, Mingrui Xia^{1,2,3}, Xuhong Liao⁴, Jiaying Zhang^{1,2,3}, Dinggang Shen^{5,6}, Li Wang⁷, Yong He^{1,2,3,8*}

¹ State Key Laboratory of Cognitive Neuroscience and Learning, Beijing Normal University, Beijing 100875, China

² Beijing Key Laboratory of Brain Imaging and Connectomics, Beijing Normal University, Beijing 100875, China

³ IDG/McGovern Institute for Brain Research, Beijing Normal University, Beijing 100875, China

⁴ School of Systems Science, Beijing Normal University, Beijing 100875, China

⁵ School of Biomedical Engineering, ShanghaiTech University, Shanghai 201210, China

⁶ Department of Research and Development, Shanghai United Imaging Intelligence Co., Ltd., Shanghai 200030, China

⁷ Department of Radiology and BRIC, University of North Carolina at Chapel Hill, NC 27599, USA

⁸ Chinese Institute for Brain Research, Beijing 102206, China

* Corresponding authors:

Tengda Zhao, Ph.D., E-mail: tengdazhao@bnu.edu.cn

Yong He, Ph.D., E-mail: yong.he@bnu.edu.cn

Manuscript information: 28 text pages, 6 figures, 6 tables.

Abstract

Precise segmentation of infant brain MR images into gray matter (GM), white matter (WM), and cerebrospinal fluid (CSF) is essential for studying neuroanatomical hallmarks of early brain development. However, for 6-month-old infants, the extremely low-intensity contrast caused by inherent myelination hinders accurate tissue segmentation. Existing convolutional neural networks (CNNs) based segmentation model for this task generally employ single-scale symmetric convolutions, which are inefficient for encoding the isointense tissue boundaries in limited samples of baby brain images. Here, we propose a 3D mixed-scale asymmetric convolutional segmentation network (3D-MASNet) framework for brain MR images of 6-month-old infant. We replaced the traditional convolutional layer of an existing to-be-trained network with a 3D mixed-scale convolution block consisting of asymmetric kernels (MixACB) during the training phase and then equivalently converted it into the original network. Five canonical CNN segmentation models were evaluated using both T1- and T2-weighted images of 23 6-month-old infants from iSeg-2019 datasets, which contained manual labels as ground truth. MixACB significantly enhanced the average accuracy of all five models and obtained the largest improvement in the fully convolutional network model (CC-3D-FCN) and the highest performance in the Dense U-Net model. This approach further obtained Dice coefficient accuracies of 0.931, 0.912, and 0.961 in GM, WM, and CSF, respectively, ranking first among 30 teams on the validation dataset of the iSeg-2019 Grand Challenge. Thus, the proposed 3D-MASNet can improve the accuracy of existing CNNs-based segmentation models as a plug-and-play solution that offers a promising technique for future infant brain MRI studies.

Keywords: infant brain, MRI, convolutional neural networks, mixed-scale convolution

1. Introduction

Modern advanced magnetic resonance (MR) imaging on the human baby brain enables researchers to chart the normal and abnormal early brain development of local regions, connections, and network topologies (Cao et al., 2017; Hazlett et al., 2017; Wang et al., 2019a; Wen et al., 2019; Xu et al., 2019; Zhao et al., 2019). The accurate image segmentation into gray matter (GM), white matter (WM), and cerebrospinal fluid (CSF) is important for producing quantitative and comparable metrics of brain tissues for early brain studies (Li et al., 2019). Notably, tissue segmentation of 6-month-old infants is extremely challenging due to the isointense phase in which the opposing changes in intensity of GM and WM lead to indistinguishable image tissue boundary (Fig. 1). An effective segmentation approach, often regarded as the gold standard, is manual annotation based on longitudinal and multimodality data (Wang et al., 2019b). However, this approach is limited by high labor costs, specialized expert knowledge, and high inter- and intra-rater variations (Makropoulos et al., 2018). Developing fast, automatic, and accurate brain segmentation algorithms is a crucial and continuous goal for MR images of infants at 6 months of age.

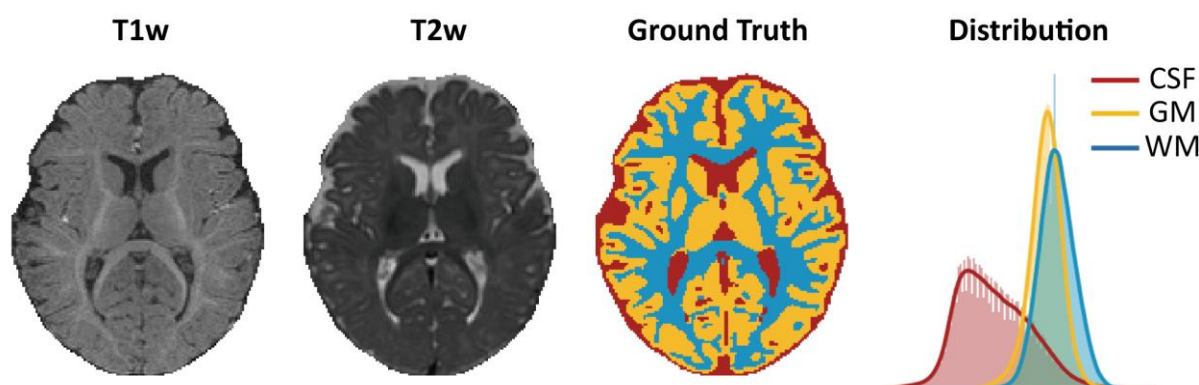


Figure 1. Data of a 6-month-old infant from the training set in iSeg-2019. The isointense brain appearance of an axial slice in T1-weighted (T1w) and T2-weighted (T2w) images. An axial view of the manual segmentation label (ground truth) and the corresponding brain tissue intensity distribution of the T1w image (distribution).

1.1. Classical machine learning methods with hand-crafted features exhibit reasonable performance.

In past years, machine learning-based brain segmentation methods leveraging multimodal images have achieved better performance than traditional atlas-based methods for MR images of 6-month-old infants (Wang et al., 2014; Wang et al., 2012b). Specifically, Wang et al. obtained reasonable performance by utilizing random forest classifiers to effectively integrate context features of multimodal information (Wang et al., 2015) and further by introducing prior anatomical tissue knowledge (Wang et al., 2018a). Additionally, also based on multimodal images, Sanroma et al. combined multi-atlas label fusion (MLF) approaches (Wang et al., 2012a; Wu et al., 2014) with learning-based methods (Hao et al., 2014; Moeskops et al., 2015) to achieve an improved segmentation accuracy (Sanroma et al., 2018). However, these methods considerably relied on hand-crafted features of a single image modality, such as Harr-like or gaussian convolved designs, making it difficult to identify critical complementary information in images from multiple modalities (Sanroma et al., 2018; Wang et al., 2015; Wang et al., 2018a; Wang et al., 2014).

1.2. Deep learning-based methods that automatically extract effective hierarchy features improve results.

Recently, advances in deep learning techniques (LeCun et al., 2015) have motivated researchers to refine many canonical convolutional neural networks (CNNs) (Bui et al., 2019; Long et al., 2015; Nie et al., 2018; Nie et al., 2016; Zhang et al., 2015), such as DenseNets (Huang et al., 2017) and U-Net (Ronneberger et al., 2015), for isointense brain MR image segmentation tasks on 6-month-old infants (Nie et al., 2018; Nie et al., 2016; Zhang et al., 2015) by adjusting or adding specific connectional pathways within or across neural layers. These approaches enhance the effective delivery and fusion of the semantic information in multimodal features and have achieved improved performance compared to classic machine learning approaches. Specifically, Bui et al. improved DenseNets by concatenating fine and coarse feature maps from multiple densely connected blocks and won the iSeg-2017 competition (Bui et al., 2019). Dolz et al. proposed a semi-dense network by directly connecting all of the convolutional layers to the end of the network (Dolz et al., 2020) and further extended it into a HyperDenseNet by adding dense connections between multimodal network paths (Dolz et al., 2018). Similarly, Zeng et al.

modified the classical U-Net network by constructing multi-encoder paths for each modality to effectively extract targeted high-level information (Zeng and Zheng, 2018). Wang et al. designed a global aggregation block in the U-Net model to consider global information in the decoder path of feature maps (Wang et al., 2020). Interestingly, inspired by the superiority of DenseNets and U-Net, the densely connected U-Net (DU-Net) model with a combination of these two types of networks was proposed for both tissue segmentation and autism diagnosis (Wang et al., 2018b). To promote the development of 6-month-old infant brain MRI segmentation, the MICCAI iSeg grand challenge was established (iSeg-2017/2019) and has become a benchmark in this field (Sun et al., 2021; Wang et al., 2019b).

1.3. Limitations in current CNN-based segmentation frameworks.

Although great efforts have been made, limitations still exist in the current CNN-based segmentation methods for the infant brain. First, all these CNN-based methods employ a single-scale convolution operation while underrating the fine-grained tissue edge information at multiple levels. Adult brain segmentation frameworks (de Brebisson and Montana, 2015; Kamnitsas et al., 2017) have tried to introduce multi-scale information by resampling input patches into different resolutions. These approaches are unsuitable for infant brain segmentation task because the small sizes and fuzzy tissue appearance of baby brain image may cause large loss of fine-grained features in low-resolution patches. The multi-resolution pathways also need additional trainable parameters that are expensive for the insufficient labeled samples in infant brain segmentation. Second, all these models use traditional symmetric convolution operators that uniformly apply grid sampling of the multimodal feature maps. This type of convolution may underemphasize the knowledge learned in skeleton part of kernels, which has been proved more valuable than corner positions (Ding et al., 2019). Third, all previous methods focused on improving network architectures, such as modality fusion pathways (Dolz et al., 2018; Zeng and Zheng, 2018), interlayer connections (Bui et al., 2019; Dolz et al., 2020; Dolz et al., 2018) or information integration modules (Wang et al., 2020). These network designs need seasoned expertise experiences and underrate the value of effective feature extractions at convolutional filter levels. Fourth, integration of these approaches for a better performance is difficult due to their variable network layouts, time-consuming hyperparameter tuning and excessive graphics processing unit (GPU) memory usage (Dolz et al., 2018; Wang et al., 2020).

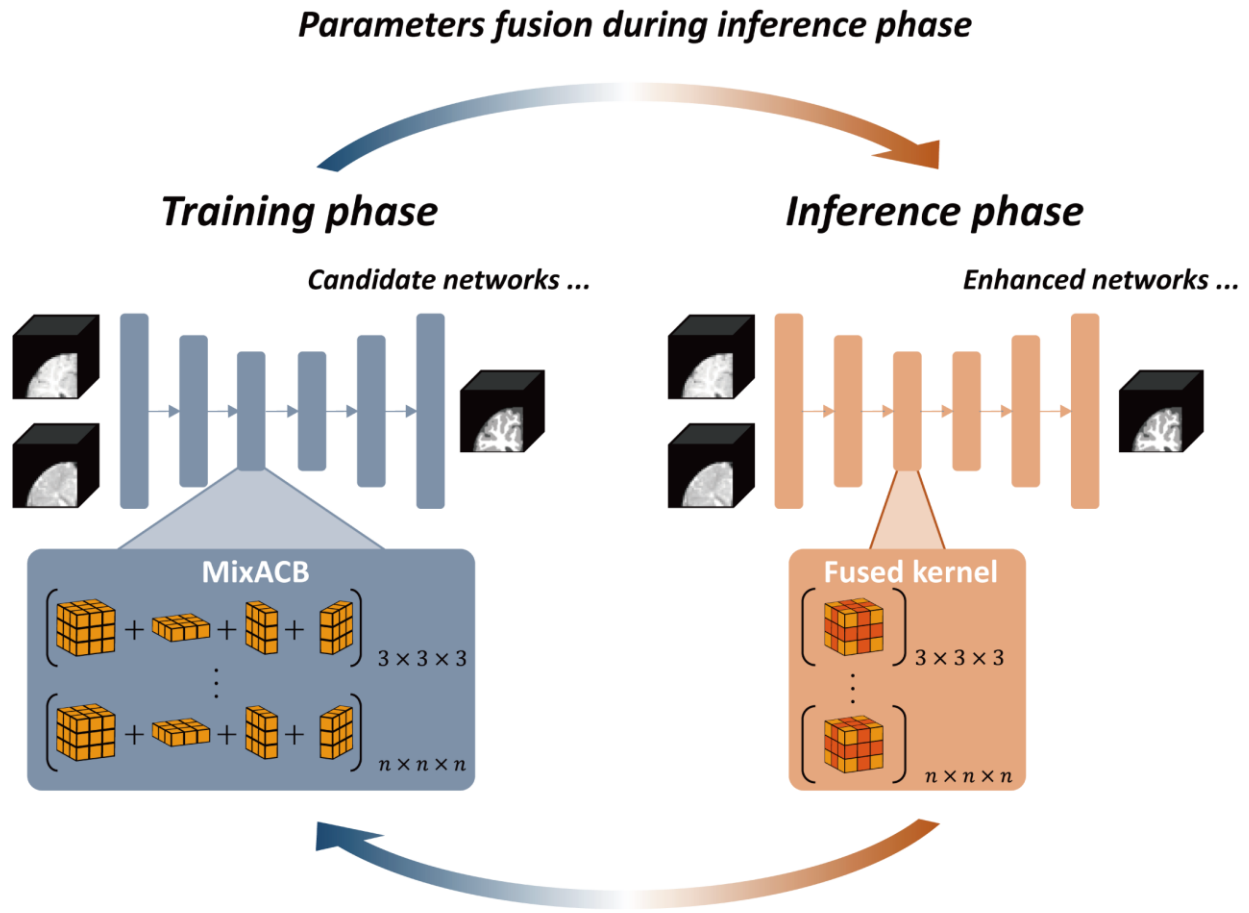
1.4. Our contribution.

Our goal is to obtain a CNN-based building block for 6-month-old infant brain image segmentation 1) that can enhance the capacity and efficiency of multi-scale feature extraction for local brain tissues of multimodal images, 2) is independent of network layouts and thus transplantable in existing segmentation models in a plug-and-play way, and 3) that can increase performance without much additional hyperparameter tuning or computational burden. In this paper, we propose a 3D mixed-scale asymmetric segmentation network (3D-MASNet) framework by embedding a well-designed 3D mixed-scale asymmetric convolution block (MixACB) into existing segmentation CNNs to perform segmentation on 6-month-old infant brain MR images (Fig. 2). Specifically, MixACB splits the input feature map into multiple groups and applies multiple 3D asymmetric convolutions with different kernel sizes independently for each group. To further decrease the computational burden during the inference phase, the parameters of each group of asymmetric convolutions in MixACB were further fused. We first evaluated the effectiveness of the MixACB on five canonical CNN networks using the iSeg-2019 training dataset. We next compared the performance of our method with that of 29 approaches proposed in the MICCAI iSeg-2019 Grand Challenge on the iSeg-2019 validation dataset. The experimental results revealed that the MixACB significantly improved the segmentation accuracy of various CNNs, among which DU-Net (Wang et al., 2018b) with MixACB achieved the best-enhanced average performance and obtained the highest Dice coefficients of 0.931 in GM, 0.912 in WM, and 0.961 in CSF, ranking first in the iSeg-2019 Grand Challenge. All codes are publicly available at <https://github.com/RicardoZiTseng/3D-MASNet>.

2. Methods and Implementations

2.1. 3D mixed-scale asymmetric convolution block (MixACB)

We constructed the 3D-MASNet by replacing every convolutional layer of a candidate network with the MixACB, which consists of 3D asymmetric convolutions with different kernel sizes. The multiple layers in the MixACB were trained separately and then summed to fuse the learned features during the training phase. During the inference phase, the parameters of MixACB are equivalently fused to produce identical outputs as the training phase (Fig. 2).



Replace conv with MixACB during training phase

Figure 2. Overview of the 3D-MASNet framework. For a candidate network, we replace its traditional convolutional layers with MixACB during the training phase. Once the training process is complete, we fuse the parameters of MixACB to obtain an enhanced model containing fewer parameters.

2.1.1. Mathematical formulation of basic 3D convolution

Consider a feature map $I \in \mathbb{R}^{U \times V \times S \times C}$ with a spatial resolution of $U \times V \times S$ as input and a feature map $O \in \mathbb{R}^{R \times T \times Q \times K}$ with a spatial resolution of $R \times T \times Q$ as output of a convolutional layer with a kernel size of $H \times W \times D$ and K filters. Then, each filter's kernel is denoted as $F \in \mathbb{R}^{H \times W \times D \times C}$, and the operation of the convolutional layer with a batch normalization (BN) layer can be formulated as follows:

$$\begin{aligned}
 O_{:::,j} &= \left(\sum_{k=1}^C I_{:::,k} * F_{:::,k}^{(j)} - \mu_j \right) \cdot \frac{\gamma_j}{\sigma_j} + \beta_j \\
 &= \left(\sum_{k=1}^C I_{:::,k} * \frac{\gamma_j}{\sigma_j} F_{:::,k}^{(j)} \right) - \frac{\mu_j \gamma_j}{\sigma_j} + \beta_j
 \end{aligned} \tag{1}$$

where $*$ is the 3D convolution operator, $I_{:::,k}$ is the k^{th} channel of the input feature map I , $F_{:::,k}^{(j)}$ is the k^{th} channel of the j^{th} filter's kernel, μ_j and σ_j are the channel-wise mean value and standard deviation value, respectively, γ_j and β_j are the scaling factor and bias term to restore the representation ability of the network, respectively.

2.1.2. Fusing 3D asymmetric convolution parameters for an equivalent conversion

In this paper, 3D asymmetric convolutions contain 4 parallel convolutional branches. The input feature maps are fed into the 4 layers, and the outputs of these branches are summed to obtain the final output of 3D asymmetric convolutions (Fig. 3A). Due to the additivity of convolutional kernels, the kernels of the four branches can be fused to obtain an equivalent kernel in a 3D convolutional layer to produce the same output, which can be formulated as the following equation:

$$I * F + I * F + I * F + I * \bar{F} = I * (F \oplus F \oplus F \oplus \bar{F}) = I * F' \tag{2}$$

where I is an input feature map, F , F , F and \bar{F} are the 4 layer's kernels of 3D asymmetric convolutions. $*$ is an elementwise operator that performs parameter addition on the corresponding positions, and F' is the equivalent fused kernel of the 4 layers' kernels.

Once the training process of the 3D asymmetric convolution was complete, we equivalently fused the parameters of the four parallel layers to retain the same computations as the original network while improving network capacity. Here, we took a kernel size of 3 as an example. We first fused the BN parameters into the convolutional kernel term and bias term following Eq. (1). Then, we further fused the four parallel kernels by adding the asymmetric kernels onto the skeletons of the cubic kernel. Formally, we denote $F^{(j)}$ as the j^{th} filter at the $1 \times 3 \times 3$, $3 \times 1 \times 3$ and $3 \times 3 \times 1$ layer, respectively. Hence, we obtain the following formulas:

$$F'^{(j)} = \frac{\gamma_j}{\sigma_j} F^{(j)} \oplus \frac{\tilde{\gamma}_j}{\tilde{\sigma}_j} \tilde{F}^{(j)} \oplus \frac{\hat{\gamma}_j}{\hat{\sigma}_j} \hat{F}^{(j)} \oplus \frac{\bar{\gamma}_j}{\bar{\sigma}_j} \bar{F}^{(j)} \tag{3}$$

$$b'_j = -\frac{\mu_j \gamma_j}{\sigma_j} - \frac{\tilde{\mu}_j \tilde{\gamma}_j}{\tilde{\sigma}_j} - \frac{\hat{\mu}_j \hat{\gamma}_j}{\hat{\sigma}_j} - \frac{\bar{\mu}_j \bar{\gamma}_j}{\bar{\sigma}_j} + \beta_j + \tilde{\beta}_j + \hat{\beta}_j + \bar{\beta}_j \quad (4)$$

Then, we can write any output of j^{th} filter as:

$$O_{:,j} + \tilde{O}_{:,j} + \hat{O}_{:,j} + \bar{O}_{:,j} = \sum_{k=1}^C I_{:,k} * F_{:,k}^{(j)} + b'_j \quad (5)$$

where $O_{:,j}$, $\tilde{O}_{:,j}$, $\hat{O}_{:,j}$ and $\bar{O}_{:,j}$ are the outputs of the original $3 \times 3 \times 3$, $1 \times 3 \times 3$, $3 \times 1 \times 3$ and $3 \times 3 \times 1$ branch, respectively.

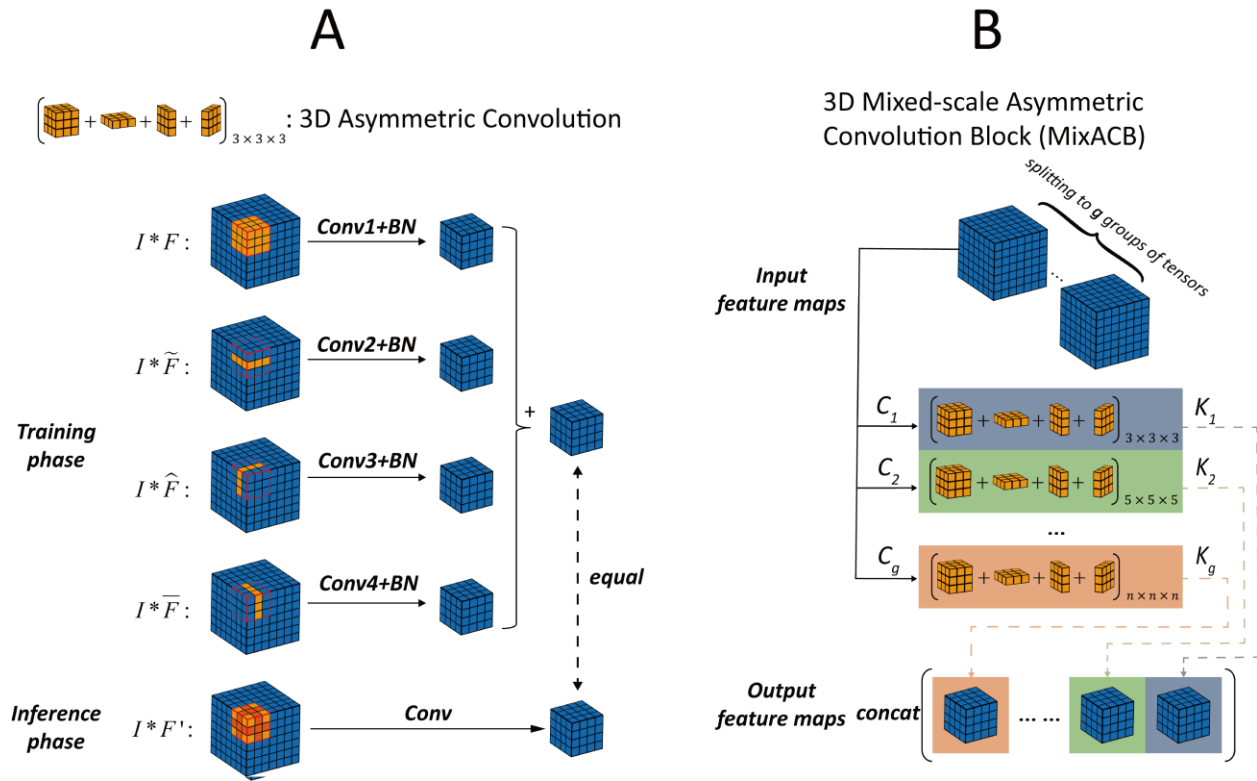


Figure 3. (A) Diagram of 3D asymmetric convolution (taking a kernel size of 3 as an example), which has four convolutional layers during the training phase and one convolutional layer once kernel parameters have been fused during the inference phase. (B) Diagram of MixACB, which is composed of multiple 3D asymmetric convolutions with different kernel sizes. MixACB splits input feature maps into several groups, applies asymmetric convolution on each group of feature maps, and then concatenates each group's output as the output feature maps.

2.1.3. Constructing MixACB by multiple 3D asymmetric convolutions with different scales

To process the input feature map at different scales of detail, we propose the MixACB by mixing multiple 3D asymmetric convolutions with different kernel sizes, as illustrated in Fig. 3B. Since

directly adopting multiple 3D asymmetric convolutions can increase the models' computational burden, we leverage the grouped convolution approach by splitting original input feature maps into groups and apply 3D asymmetric convolution independently in each input feature map's group. Assume that we split the input feature maps into g groups of tensors such that their total number of channels is equal to the original feature maps' channels: $C_1 + C_2 + \dots + C_g = C$; similarly, the output feature maps also have g groups: $K_1 + K_2 + \dots + K_g = K$. We denote $I^{<i>} \in \mathbb{R}^{U \times V \times S \times C_i}$ as the i^{th} group of input, $O^{<i>} \in \mathbb{R}^{R \times T \times Q \times K_i}$ as the MixACB's i^{th} group output, and $F^{<i>} \in \mathbb{R}^{H_i \times W_i \times D_i \times C_i}$ as the equivalent kernel of the i^{th} group of the 3D asymmetric convolution whose equivalent kernel size is $H_i \times W_i \times D_i$. Thus, we have following equations:

$$O_{\dots, j}^{<i>} = \left(\sum_{q=1}^{C_i} I_{\dots, q}^{<i>} * F_s^{<i> \langle j \rangle} \right) + b_j^{<i>} \quad (6)$$

s.t. $1 \leq i \leq g, \quad 1 \leq j \leq K_i$

The final output of MixACB is the concatenation of all groups' outputs:

$$O = \text{concat} \left(O^{<1>}, O^{<2>}, \dots, O^{<g>} \right) \quad (7)$$

In this paper, we only split the input and output feature maps into 2 groups, and we define the mix ratio as the ratio between C_1 and C_2 . For simplicity, the ratio between K_1 and K_2 is set to be equal to the mix ratio. For the construction of each MixACB, we set a kernel size of 3 for the 1st group of convolutions and a kernel size of 5 for the 2nd group of convolutions, with the mix ratio set to 3:1.

2.2. Candidate CNNs for the evaluation of the MixACB on 6-month-old infant brain image segmentation

We choose five representative networks to evaluate the effectiveness of the 3D-MixACB in improving the segmentation performance, including BuiNet (Bui et al., 2019), 3D-UNet (Çiçek et al., 2016), convolution and concatenate 3D fully convolutional network (CC-3D-FCN) (Nie et al., 2018), non-local U-Net (NLU-Net) (Wang et al., 2020) and DU-Net (Wang et al., 2018b). Notably, these five networks are either variants of the U-type architecture (3D U-Net, NLU-Net and DU-Net) or the FCN-type architecture (BuiNet and CC-3D-FCN) and encompass major CNN frameworks in infant brain segmentation. After replacing their original convolution layers

with the 3D-MixACB design, we followed the training configurations set in the candidate CNN's release codes (Table 1) and adopted the Adam optimizer (Kingma and Ba, 2015) to update these models' parameters. Except for the CC-3D-FCN, which used the Xavier algorithm (Glorot and Bengio, 2010) to initialize network weights, all other networks adopted the He initialization method (He et al., 2015). The configuration parameters are as follows:

(1) BuiNet adopted four dense blocks consisting of four $3 \times 3 \times 3$ convolutional layers for feature extraction. Transition blocks were applied between every two dense blocks to reduce the feature map resolutions. 3D up-sampling operations were used after each dense block for feature map recovery, and these upsampled features were concatenated together. (2) 3D-UNet has 4 levels of resolution, and each level adopts one $3 \times 3 \times 3$ convolutions, which is followed by BN and a rectified linear unit (ReLU). The $2 \times 2 \times 2$ max pooling and the $2 \times 2 \times 2$ transposed convolution, each with a stride of 2, are employed for resolution reduction and recovery. Feature maps of the same level of both paths were summed. (3) CC-3D-FCN used 6 groups of $3 \times 3 \times 3$ convolutional layers for feature extraction, in which the $2 \times 2 \times 2$ max pooling with a stride of 2 were adopted between two groups of layers. The $1 \times 1 \times 1$ convolution with a stride of 1 was added between two groups with the same resolution for feature fusion. (4) DU-Net used 7 dense blocks to construct the encoder-decoder structure with 4 levels of resolution and leveraged transition down blocks and transition up blocks for down-sampling and up-sampling, respectively. Unlike the implementations in (Wang et al., 2018b), the bottleneck layer is introduced into the dense block to constrain the rapidly increasing number of feature maps, and the transition down block consisted of two $3 \times 3 \times 3$ convolutions, each followed by BN and ReLU. In addition, we used the $1 \times 1 \times 1$ convolution followed by a softmax activation function in the last layer. (5) NLU-Net leveraged five different kinds of residual blocks to form the U-type architecture with 3 levels of resolution. BN with the ReLU6 activation function was adopted before each $3 \times 3 \times 3$ convolution. The global aggregation block replaced the two convolutional layers of the input residual block to form the bottom residual block for the integration of global information.

We fed the same multimodal images into these five networks and employed the same inference strategy. We extracted overlapping patches with the same size as that used during the training phase. The overlapping step size had to be smaller than or equal to the patch length size to form the whole volume. Following the common practice in (Bui et al., 2019; Nie et al., 2018;

Wang et al., 2018b; Wang et al., 2020), we set the step size to 8. Since the effect of the overlapping step size in the proposed framework remains unknown, we further evaluated it in section 3.3. Voxels inside the overlapping regions were averaged.

Table 1. Training strategy of each candidate network

Candidate Network	Training Batch Size	Training/Inference Patch Size	Learning Rate Schedule
BuiNet	4	64	Train for 20,000 iterations. The initial learning rate is set to $2e-4$ and is decreased by a factor of 0.1 every 5000 iterations.
3D-UNet	10	32	Train for 80 epochs for a total of 5000 patches that are randomly extracted per epoch. The learning rate is decreased every 20 epochs and is set to $3e-4$, $1e-4$, $1e-5$ and $1e-6$. Train for 80 epochs for a total of 5000 patches that are randomly extracted per epoch. The learning rate is decreased every 20 epochs and is set to $3e-4$, $1e-4$, $1e-5$ and $1e-6$.
CC-3D-FCN	10	32	The same as 3D-UNet.
NLU-Net	5	32	Train for 80 epochs for a total of 5000 patches that are randomly extracted per epoch. The learning rate is set to $1e-3$.
DU-Net	16	32	The cosine annealing strategy with a maximum learning rate of $3e-4$ and a minimum learning rate of $1e-6$ is adopted. The model is trained for 500 epochs and a total of 1000 patches are randomly extracted at each epoch.

3. Experiments and Results

3.1. iSeg-2019 dataset and image preprocessing

Twenty-three isointense phase infant brain MRIs, including T1w and T2w images, were offered by the iSeg-2019 (<http://iseg2019.web.unc.edu/>) organizers from the pilot study of the Baby Connectome Project (BCP) (Howell et al., 2019). All the infants were term born (40 ± 1 weeks of gestational age) with an average scan age of 6.0 ± 0.5 months. All experimental procedures were approved by the University of North Carolina at Chapel Hill and the University of Minnesota Institutional Review Boards. Detailed imaging parameters and preprocessing steps that were implemented are listed in (Sun et al., 2021). Before cropping the MR images into patches, we normalized the T1w and T2w images by subtracting the mean value and dividing by the standard

deviation value.

The iSeg-2019 organizers offered the ground truth labels, which were obtained by a combination of initial automatic segmentation using the infant brain extraction and analysis toolbox (iBEAT) (Dai et al., 2013) on follow-up 24-month scans of the same baby and manual editing using ITK-SNAP (Yushkevich et al., 2006) under the guidance of an experienced neuroradiologist. The MR images of 10 infants with manual labels were provided for model training and validation. The images of 13 infants without labels were provided for model testing. The testing results were submitted to the iSeg-2019 organizers for quantitative measurements.

3.2. Evaluation metrics

We employed the Dice coefficient (DICE), modified Hausdorff distance (MHD) and average surface distance (ASD) to evaluate the model performance on segmenting 6-month-old infant brain MR images.

3.2.1. Dice coefficient

Let A and B be the manual labels and predictive labels, respectively. The DICE can be defined as:

$$DICE(A, B) = \frac{2|A \cap B|}{|A| + |B|} \quad (8)$$

where $|\cdot|$ denotes the number of elements of a point set. A higher DICE indicates a larger overlap between the manual and predictive segmentation areas.

3.2.2. Modified Hausdorff distance

Let C and D be the sets of voxels within the manual and predictive segmentation boundary, respectively. MHD can be defined as:

$$MHD(C, D) = \max \{h(C, D), h(D, C)\} \quad (9)$$

where $h(C, D) = \frac{1}{N_c} \sum_{c \in C} d(c, D)$, and $d(c, D) = \min_{d \in D} \|c - d\|$ with $\|\cdot\|$ representing the

Euclidean distance. We follow the calculation described in (Wang et al., 2020) by computing the average MHD based on the three different vectorization directions to obtain a direction-independent evaluation metric. A smaller MHD coefficient indicates greater similarity between manual and predictive segmentation contours.

3.2.3. Average surface distance

The ASD is defined as:

$$ASD(C, D) = \frac{1}{2} \cdot \left(\frac{\sum_{v_i \in S_C} \min_{v_j \in S_D} \|v_i - v_j\|}{\sum_{v_i \in S_C} 1} + \frac{\sum_{v_j \in S_D} \min_{v_i \in S_C} \|v_j - v_i\|}{\sum_{v_j \in S_D} 1} \right) \quad (10)$$

where S_C and S_D represent the surface meshes of C and D , respectively. A smaller ASD coefficient indicates greater similarity between cortical surfaces reconstructed from manual and predictive segmentation maps.

3.3. Exploring the effectiveness of the MixACB

We performed several experiments to evaluate the effectiveness of the MixACB, including 1) ablation tests on five representative segmentation networks (section 2.2); 2) comparisons with state-of-the-art approaches in iSeg-2019; 3) component analysis of MixACB; and 4) validation of the impact of the overlapping step size.

3.3.1. Performance improvement on five representative CNN architectures

For a given network architecture without the MixACB design, we regarded it as the baseline model and further transformed it into a 3D-MASNet design. All pairs of the baseline models and their corresponding 3D-MASNet followed the training strategies described in Table 1. To balance the training and testing sample sizes, we adopt a 2-fold cross-validation (one fold with five random selected participants for training and the left for testing) for model evaluation on the iSeg-2019 training dataset. Table 2 and Table 3 and Fig. 4 show that the performance of all the models was significantly improved across almost all tissue types in terms of the DICE and MHD, which demonstrates the effectiveness of the MixACB on a wide range of CNN layouts. Specifically, DU-Net with the MixACB achieved the highest average DICE of 0.928 and the lowest average MHD value of 0.436; CC-3D-FCN with the MixACB gained the largest DICE improvement and reached a higher average DICE than that attained by BuiNet, which was a champion solution in the MICCAI iSeg-2017 grand challenge, indicating that a simple network could reach excellent performance by advanced convolution designs. Fig. 5 further provides a visual segmentation comparison between networks with and without the MixACB. The MixACB could effectively correct misclassified voxels which are indicated by red squares.

Table 2. Ablation study performed by comparing the segmentation accuracy between different models and their corresponding 3D-MASNet in terms of DICE by 2-fold cross validation.

Network	CSF		GM		WM		Avg	
	Baseline	MixACB	Baseline	MixACB	Baseline	MixACB	Baseline	MixACB
BuiNet	0.938±0.010	0.938±0.011	0.905±0.007	0.908*±0.007	0.888±0.014	0.892*±0.013	0.910±0.007	0.912*±0.007
3D-UNet	0.940±0.010	0.942*±0.008	0.907±0.007	0.909*±0.007	0.889±0.014	0.892*±0.015	0.912±0.007	0.914*±0.008
CC-3D-FCN	0.923±0.010	0.942*±0.008	0.910±0.006	0.911±0.007	0.892±0.013	0.894*±0.013	0.908±0.006	0.915*±0.006
NLU-Net	0.947±0.009	0.949*±0.008	0.918±0.007	0.919±0.006	0.903±0.012	0.904±0.014	0.922±0.006	0.924*±0.006
DU-Net	0.951±0.008	0.953*±0.008	0.922±0.007	0.923*±0.007	0.907±0.015	0.907±0.015	0.927±0.007	0.928*±0.008

Note that the best values are highlighted in bold font. “Baseline” denotes that the corresponding model adopted the standard convolutional operation; “MixACB” denotes that the corresponding model was transformed into 3D-MASNet; “*” denotes that the difference between baseline and 3D-MASNet is statistically significant (p<0.05).

Table 3. Ablation study performed by comparing the segmentation accuracy between different models and their corresponding 3D-MASNet in terms of MHD by 2-fold cross validation.

Network	CSF		GM		WM		Avg	
	Baseline	MixACB	Baseline	MixACB	Baseline	MixACB	Baseline	MixACB
BuiNet	0.308±0.024	0.307±0.023	0.659±0.048	0.649*±0.045	0.493±0.043	0.485*±0.042	0.487±0.035	0.480*±0.034
3D-UNet	0.299±0.022	0.293*±0.020	0.658±0.050	0.651*±0.046	0.490±0.046	0.485*±0.042	0.483±0.036	0.476*±0.033
CC-3D-FCN	0.348±0.022	0.292*±0.023	0.649±0.047	0.645*±0.048	0.485±0.046	0.480*±0.046	0.494±0.034	0.473*±0.034
NLU-Net	0.278±0.022	0.270*±0.020	0.619±0.043	0.615*±0.040	0.461±0.040	0.460±0.037	0.453±0.032	0.448*±0.030
DU-Net	0.261±0.021	0.254*±0.022	0.605±0.046	0.601*±0.047	0.452±0.041	0.452±0.043	0.439±0.032	0.436*±0.034

Note that the best values are highlighted in bold font. “Baseline” denotes that the corresponding model adopted the standard convolutional operation; “MixACB” denotes that the corresponding model was transformed into 3D-MASNet; “*” denotes that the difference between baseline and 3D-MASNet is statistically significant (p<0.05).

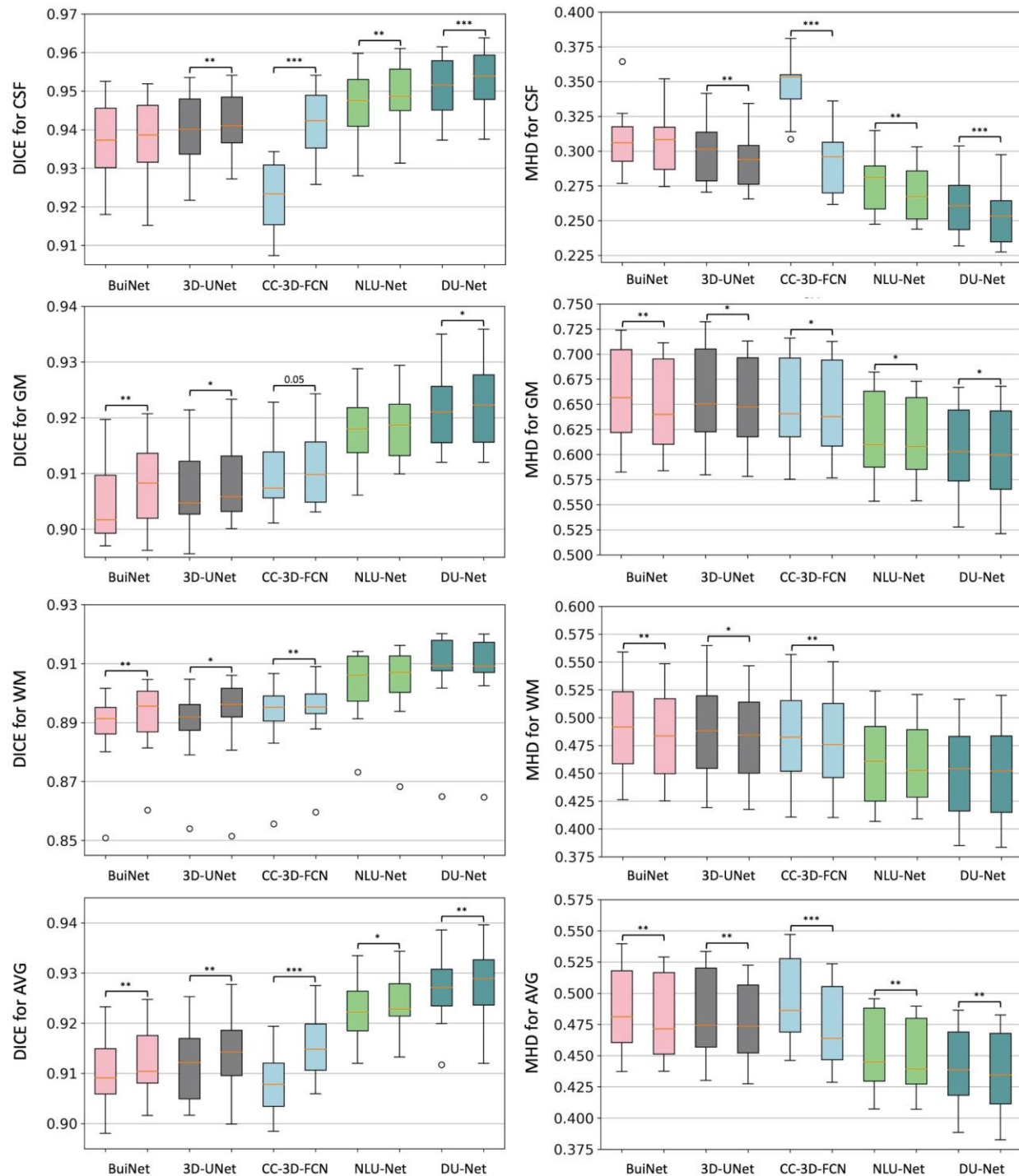


Figure 4. Box plot of the segmentation performance improvement on five candidate CNN architectures in the 3D-MASNet framework. The first column shows the measurement of DICE to represent the segmentation accuracy for each tissue type. The second column shows the results of MHD. In each subgraph, we use two neighbor box plots to represent a candidate model (first plot) and its corresponding 3D-MASNet (second plot). The significance of model comparison is evaluated by 2-fold cross-validation. “**” denotes that $0.01 \leq p < 0.05$, “***” denotes that $0.001 \leq p < 0.01$, and “****” denotes that $p < 0.001$.

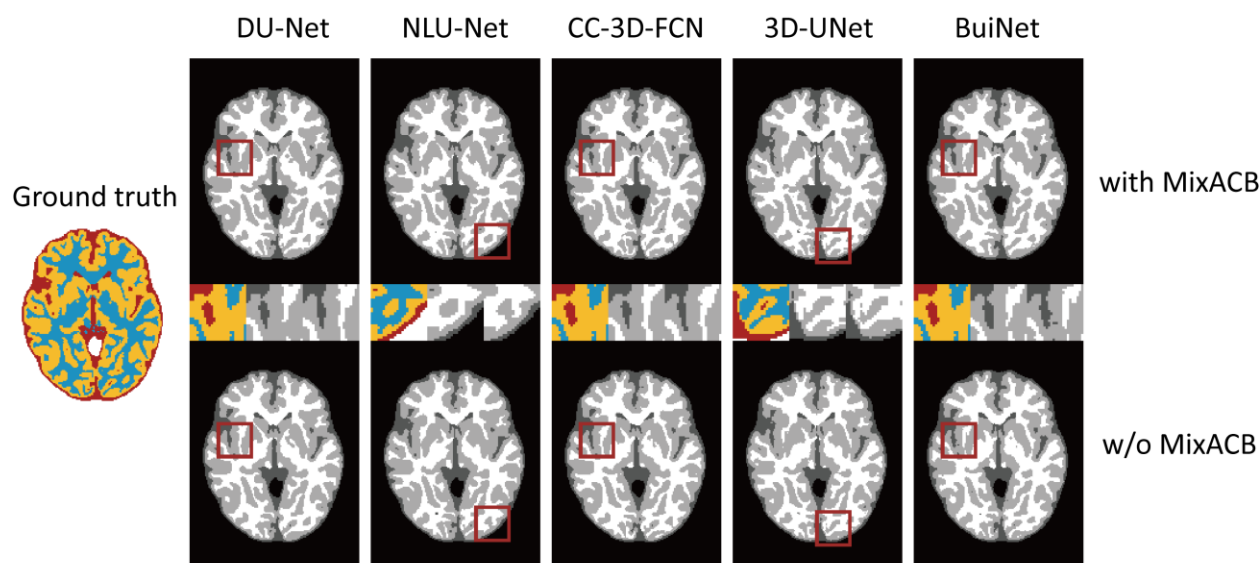


Figure 5. Visualization of the segmentation results on different models with (w) and without (w/o) the MixACB. The ground truth map is shown in color, and CNNs-based segmentation maps are shown in the gray scale. The regions in the red square are magnified in the middle row following an order from with MixACB to without MixACB.

3.3.2. Comparison with state-of-the-art methods on iSeg-2019

Since DU-Net, which was combined with MixACB, has achieved the highest accuracy among all candidate models, we compared it with methods developed by the 29 remaining teams that participated in the iSeg-2019 challenge. We employed a majority-voting strategy on 10 trained networks' outputs to improve the model generalization.

Table 4 reports the segmentation results achieved by our proposed method and those of other teams' methods that ranked in the top 4 on the validation dataset of the iSeg-2019. The mean DICE, MHD value and ASD value are presented for CSF, GM, and WM, representatively. Compared with other teams, our method yielded the highest DICE and lowest ASD value for the three brain tissues in the validation test of iSeg-2019, with comparable MHD values. The superior average value of the 3 types of brain tissues also indicates that our method has the best overall performance.

Table 4. Comparison of segmentation performance of the proposed method and the methods of the top-4 ranked teams on the 13 validation infant MRI images of iSeg-2019.

Method	CSF			GM			WM			AVG		
	DICE	MHD	ASD	DICE	MHD	ASD	DICE	MHD	ASD	DICE	MHD	ASD
Brain_Tech	0.961	8.873	0.108	0.928	5.724	0.300	0.911	7.114	0.347	0.933	7.237	0.252
FightAutism	0.960	9.233	0.110	0.929	5.678	0.300	0.911	6.678	0.341	0.933	7.196	0.250
OxfordIBME	0.960	8.560	0.112	0.927	5.495	0.307	0.907	6.759	0.353	0.931	6.938	0.257
QL111111	0.959	9.484	0.114	0.926	5.601	0.307	0.908	7.028	0.353	0.931	7.371	0.258
Proposed	0.961	9.293	0.107	0.931	5.741	0.292	0.912	7.111	0.332	0.935	7.382	0.244

Note that the best values are highlighted in bold font.

Table 5. Ablation study performed by comparing the segmentation accuracy in different mix ratios by 2-fold cross validation.

Mix Ratio	CSF		GM		WM		AVG	
	DICE	MHD	DICE	MHD	DICE	MHD	DICE	MHD
1:0	0.952±0.010	0.261±0.024	0.922±0.008	0.604±0.045	0.906±0.014	0.453±0.041	0.927±0.008	0.440±0.033
1:1	0.953±0.008	0.258±0.023	0.921±0.007	0.605±0.045	0.905±0.013	0.455±0.040	0.926±0.007	0.439±0.033
3:1 (proposed)	0.953±0.008	0.254±0.022	0.923±0.007	0.601±0.047	0.907±0.015	0.452±0.043	0.928±0.008	0.436±0.034
5:1	0.953±0.009	0.257±0.025	0.922±0.008	0.601±0.047	0.907±0.015	0.452±0.042	0.926±0.008	0.437±0.034

Note that the best values are highlighted in bold font.

3.3.3. Component analysis of MixACB

We analyzed the effect of the mix ratio on model segmentation performance. Table 5 shows that segmentation accuracy reaches the highest value when the mix ratio is set to 3:1. Then, we further performed an ablation test to verify the effectiveness of each part of the proposed MixACB, as shown in Table 6. It is clear that the segmentation accuracy was improved with large variations when using different 3D asymmetric convolutions alone. Moreover, when these 3D asymmetric convolutions were mixed in scales for a MixACB design, the model was able to achieve the best performance in both DICE and MHD metrics.

Table 6. Component analysis of MixACB by 2-fold cross validation.

	CSF		GM		WM		AVG	
	DICE	MHD	DICE	MHD	DICE	MHD	DICE	MHD
CONV_3	0.951±0.0 08	0.261±0.0 21	0.922±0.0 007	0.605±0.0 46	0.907±0.0 15	0.452±0.0 41	0.927±0.0 07	0.439±0.0 32
AC_3	0.952±0.0 10	0.261±0.0 24	0.922±0.0 08	0.604±0.0 45	0.906±0.0 14	0.453±0.0 41	0.927±0.0 08	0.440±0.0 33
CONV_5	0.947±0.0 12	0.276±0.0 23	0.918±0.0 08	0.619±0.0 47	0.903±0.0 16	0.463±0.0 43	0.922±0.0 08	0.453±0.0 34
AC_5	0.952±0.0 08	0.261±0.0 22	0.920±0.0 08	0.610±0.0 46	0.904±0.0 16	0.460±0.0 43	0.925±0.0 08	0.443±0.0 33
MixACB	0.953±0.0 08	0.254±0.0 22	0.923±0.0 07	0.601±0.0 47	0.907±0.0 15	0.452±0.0 43	0.928±0.0 08	0.436±0.0 34

Note that the best values are highlighted in bold font. “CONV_3” denotes that the 3D convolution with a kernel size of 3; “AC_3” denotes that the 3D asymmetric convolution with a kernel size of 3; “CONV_5” denotes that the 3D convolution with a kernel size of 5; “AC_5” denotes that the 3D asymmetric convolution with a kernel size of 5.

3.3.4. Impact of overlapping step sizes

We further performed experiments to evaluate the effectiveness of the MixACB on overlapping step sizes, which controls the trade-off between accuracy and inference time. Based on 2-fold cross-validation, which has been done previously, we tested the overlapping impact when the step size is set to 4, 8, 16, and 32 on the DU-Net in the proposed 3D-MASNet framework. Fig. 6A and Fig. 6B present the changes in the segmentation performance in terms of DICE and MHD, respectively, with respect to different overlapping step sizes. Fig. 6C presents the changes in the average number of inference patches with respect to different overlapping step sizes. Obviously, a step size of 8 is a reasonable choice for achieving fast and accurate results.

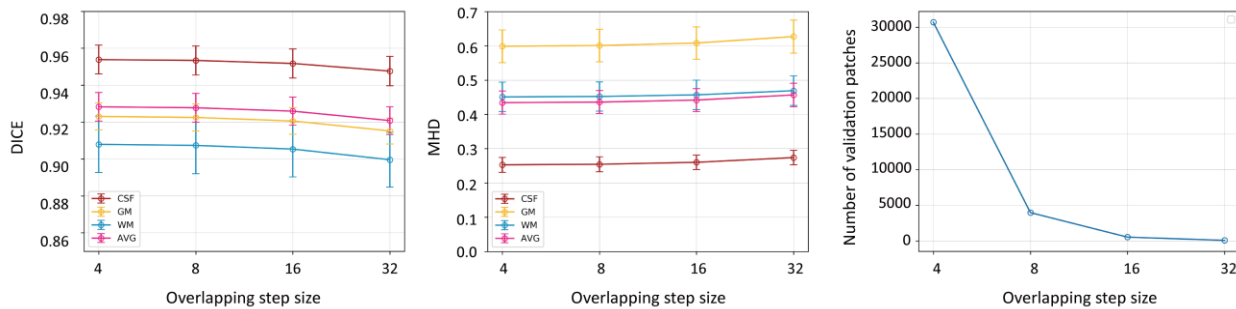


Figure 6. Changes in segmentation performance in terms of DICE (A) and MHD (B) with respect to different overlapping step sizes on 10 subjects during inference, where 2-fold cross-validation is used. (C) Changes of the average number of the 10 subjects’ patches with respect to different overlapping step sizes during inference.

4. Discussion

Instead of designing a new network architecture to segment the brain images of 6-month-old infants, we proposed a 3D-MASNet framework by replacing the standard convolutional layer with MixACB on an existing mature network and reduced model parameters by equivalently performing fusion during the inference phase. The experimental results revealed that the MixACB significantly improved the performance of several CNNs by a considerable margin, in which DU-Net with MixACB showed the best average segmentation accuracy. The proposed framework obtained the highest average DICE of 0.935 and lowest ASD of 0.244, which ranked first among all 30 teams on the validation dataset of the iSeg-2019 Grand Challenge. In addition, the CC-3D-FCN model showed the largest improvement, which indicates that a simple model could achieve a relatively better performance by implementing our convolution design.

4.1. Effectiveness of the MixACB on improving segmentation accuracy

The wide improvement in the segmentation accuracy of different models by the MixACB may be derived from several aspects. First, the mixed-scale design of MixACB enable the network to collected multiscale details of local features with different receptive fields, facilitating the integration of coarse to fine information inside the input patches. Brain segmentation networks such as DeepMedic (Kamnitsas et al., 2017) and SegNet (de Brebisson and Montana, 2015) also introduced the multiscale information into their model by feeding resliced images or labels at multiresolution into the input convolutional layers. Such approach may be a suboptimal option for infant brain segmentation since the baby brain size is quite small and the morphology details are already blurred before down-sampling. Second, the isointense intensity distribution and heterogeneous tissue contrasts hamper effective feature extraction in baby brain images. We employed the asymmetric convolution inside the MixACB to emphasize features in orthogonal directions that has been shown especially important for the representation capacity of network. Meanwhile, the asymmetric design are also shown strong robustness to image rotational distortion (Ding et al., 2019), which may help the neuronal network cope with the large individual variations in local morphology of infant brain, even though these images have been linearly aligned to standard space. Third, the mixed-scale design and asymmetric kernel enable the 3D-MASNet to learn the combination of different receptive fields adaptively in multiple pathways, further improving the representational power of the network. Notably, besides

providing better performance than the previous networks, 3D-MASNet is also more efficient than the baseline models, requiring fewer model parameters once its parameters were fused. For example, the baseline DU-Net's number of parameters is 2,492,795, while the corresponding 3D-MASNet's number of parameters is reduced to 2,341,141 during the inference phase.

4.2. Well-designed convolution operations

Recent years, some researchers have begun to shift their interests from macro network layout to micro neuron units by studying specific convolution operators rather than touching the overall network. Previous works have proposed several advanced convolution operators by combining well-designed filters, such as pyramidal convolution (PyConv), dynamic group convolution (DGC) and asymmetric convolution block (ACB). PyConv employs multiple kernels in a pyramidal way to capture different levels of image details (Duta et al., 2020); DGC equips a feature selector for each group convolution conditioned on the input images to adaptively select input features (Su et al., 2020); ACB introduces asymmetry into 2D convolution to power up the representational power of the skeleton part of kernel (Ding et al., 2019). These operators implanted into existing mature networks have achieved better performance on image classification or semantic segmentation tasks than original networks. Due to the “easy-to-plug-in” property, this type of designs could be conveniently adopted in various advanced CNNs and avoided high cost in network re-designing. However, these studies mainly concentrate on natural image tasks, few were applied on infant brain segmentation tasks. Here, we design a novel convolution block by combining three basic characteristics including 3D spatial convolution, group convolution containing mixed-scale of kernel sizes and asymmetry convolution. Due to blurred image appearance, large individual variation of brain morphology, and limited labeled sample sizes, we emphasize that effective and robust feature extraction, especially in a plug-and-play form, is essential for the infant brain segmentation task. Nevertheless, exhausting the combination of various convolution designs is beyond the scope of the article.

4.3. Limitations and future directions

The current study has several limitations. First, the patching approach may cause spatial consistency loss near boundaries. Although we adopted a small overlapping step size to relieve

this issue, it is necessary to consider further integrating guidance from global information. Second, the small sample sizes of infant-specific datasets limit the generalizability of our method for babies across geographic locations, MRI scanners and acquisition protocols. Further validation on large samples is needed. Third, image indexes, such as the fractional anisotropy derived from diffusion MRI, contain rich white matter information (Liu et al., 2007), which could be beneficial for insufficient tissue contrast (Nie et al., 2018; Zhang et al., 2015). Importantly, determining how to leverage mixed-scale asymmetric convolution to enhance specific model features needs to be further explored. Fourth, we only explored the effectiveness of MixACB when input feature maps are split into 2 groups. Further combination configurations of convolutional kernel sizes and mix ratios are warranted.

5. Conclusion

In this paper, we proposed a 3D-MASNet framework for brain MR image segmentation of 6-month-old infants, which ranked first in the iSeg-2019 Grand Challenge. We demonstrated that the designed MixACB could easily migrate to various network architectures and enable performance improvement without extra inference-time computations. This work shows great adaptation potential for further improvement in future studies on brain segmentation.

Acknowledgments

The study was supported by the National Natural Science Foundation of China (Nos. 31830034, 82021004 and 81801783), Changjiang Scholar Professorship Award (T2015027), and the China Postdoctoral Science Foundation (2020TQ0050).

Conflicting Interests

The authors have declared that no conflicting interests exist.

References

- Bui, T.D., Shin, J., Moon, T., 2019. Skip-connected 3D DenseNet for volumetric infant brain MRI segmentation. *Biomedical Signal Processing and Control* 54, 101613.
- Cao, M., Huang, H., He, Y., 2017. Developmental connectomics from infancy through early childhood. *Trends in neurosciences* 40, 494-506.
- Çiçek, Ö., Abdulkadir, A., Lienkamp, S.S., Brox, T., Ronneberger, O., 2016. 3D U-Net: learning dense volumetric segmentation from sparse annotation, *International conference on medical image computing and computer-assisted intervention*. Springer, pp. 424-432.
- Dai, Y., Shi, F., Wang, L., Wu, G., Shen, D., 2013. iBEAT: a toolbox for infant brain magnetic resonance image processing. *Neuroinformatics* 11, 211-225.
- de Brebisson, A., Montana, G., 2015. Deep neural networks for anatomical brain segmentation, *Proceedings of the IEEE conference on computer vision and pattern recognition workshops*, pp. 20-28.
- Ding, X., Guo, Y., Ding, G., Han, J., 2019. Acnet: Strengthening the kernel skeletons for powerful cnn via asymmetric convolution blocks, *Proceedings of the IEEE International Conference on Computer Vision*, pp. 1911-1920.
- Dolz, J., Desrosiers, C., Wang, L., Yuan, J., Shen, D., Ayed, I.B., 2020. Deep CNN ensembles and suggestive annotations for infant brain MRI segmentation. *Computerized Medical Imaging and Graphics* 79, 101660.
- Dolz, J., Gopinath, K., Yuan, J., Lombaert, H., Desrosiers, C., Ayed, I.B., 2018. HyperDense-Net: a hyper-densely connected CNN for multi-modal image segmentation. *IEEE transactions on medical imaging* 38, 1116-1126.
- Duta, I.C., Liu, L., Zhu, F., Shao, L., 2020. Pyramidal Convolution: Rethinking Convolutional Neural Networks for Visual Recognition.
- Glorot, X., Bengio, Y., 2010. Understanding the difficulty of training deep feedforward neural networks, *AISTATS*.
- Hao, Y., Wang, T., Zhang, X., Duan, Y., Yu, C., Jiang, T., Fan, Y., Initiative, A.s.D.N., 2014. Local label learning (LLL) for subcortical structure segmentation: application to hippocampus segmentation. *Human brain mapping* 35, 2674-2697.

- 1 Hazlett, H.C., Gu, H., Munsell, B.C., Kim, S.H., Styner, M., Wolff, J.J., Elison, J.T., Swanson,
2 M.R., Zhu, H., Botteron, K.N., 2017. Early brain development in infants at high risk for
3 autism spectrum disorder. *Nature* 542, 348-351.
- 4 He, K., Zhang, X., Ren, S., Sun, J., 2015. Delving Deep into Rectifiers: Surpassing
5 Human-Level Performance on ImageNet Classification. 2015 IEEE International
6 Conference on Computer Vision (ICCV), 1026-1034.
- 7 Howell, B.R., Styner, M.A., Gao, W., Yap, P.-T., Wang, L., Baluyot, K., Yacoub, E., Chen, G.,
8 Potts, T., Salzwedel, A., 2019. The UNC/UMN baby connectome project (BCP): an
9 overview of the study design and protocol development. *NeuroImage* 185, 891-905.
- 10 Huang, G., Liu, Z., Van Der Maaten, L., Weinberger, K.Q., 2017. Densely connected
11 convolutional networks, *Proceedings of the IEEE conference on computer vision and*
12 *pattern recognition*, pp. 4700-4708.
- 13 Kamnitsas, K., Ledig, C., Newcombe, V.F., Simpson, J.P., Kane, A.D., Menon, D.K., Rueckert,
14 D., Glocker, B., 2017. Efficient multi-scale 3D CNN with fully connected CRF for accurate
15 brain lesion segmentation. *Medical image analysis* 36, 61-78.
- 16 Kingma, D.P., Ba, J., 2015. Adam: A Method for Stochastic Optimization. *CoRR* abs/1412.6980.
- 17 LeCun, Y., Bengio, Y., Hinton, G., 2015. Deep learning. *nature* 521, 436-444.
- 18 Li, G., Wang, L., Yap, P.-T., Wang, F., Wu, Z., Meng, Y., Dong, P., Kim, J., Shi, F., Reik, I.,
19 2019. Computational neuroanatomy of baby brains: A review. *NeuroImage* 185, 906-925.
- 20 Liu, T., Li, H., Wong, K., Tarokh, A., Guo, L., Wong, S.T., 2007. Brain tissue segmentation
21 based on DTI data. *NeuroImage* 38, 114-123.
- 22 Long, J., Shelhamer, E., Darrell, T., 2015. Fully convolutional networks for semantic
23 segmentation, *Proceedings of the IEEE conference on computer vision and pattern*
24 *recognition*, pp. 3431-3440.
- 25 Makropoulos, A., Counsell, S.J., Rueckert, D., 2018. A review on automatic fetal and neonatal
26 brain MRI segmentation. *NeuroImage* 170, 231-248.
- 27 Moeskops, P., Benders, M.J., Chişă, S.M., Kersbergen, K.J., Groenendaal, F., de Vries, L.S.,
28 Viergever, M.A., Išgum, I., 2015. Automatic segmentation of MR brain images of preterm
29 infants using supervised classification. *NeuroImage* 118, 628-641.

- 1 Nie, D., Wang, L., Adeli, E., Lao, C., Lin, W., Shen, D., 2018. 3-D fully convolutional networks
2 for multimodal isointense infant brain image segmentation. IEEE transactions on
3 cybernetics 49, 1123-1136.
- 4 Nie, D., Wang, L., Gao, Y., Shen, D., 2016. Fully convolutional networks for multi-modality
5 isointense infant brain image segmentation, 2016 IEEE 13Th international symposium on
6 biomedical imaging (ISBI). IEEE, pp. 1342-1345.
- 7 Ronneberger, O., Fischer, P., Brox, T., 2015. U-net: Convolutional networks for biomedical
8 image segmentation, International Conference on Medical image computing and
9 computer-assisted intervention. Springer, pp. 234-241.
- 10 Sanroma, G., Benkarim, O.M., Piella, G., Lekadir, K., Hahner, N., Eixarch, E., Ballester, M.A.G.,
11 2018. Learning to combine complementary segmentation methods for fetal and 6-month
12 infant brain MRI segmentation. Computerized Medical Imaging and Graphics 69, 52-59.
- 13 Su, Z., Fang, L., Kang, W., Hu, D., Liu, L., 2020. Dynamic Group Convolution for Accelerating
14 Convolutional Neural Networks.
- 15 Sun, Y., Gao, K., Wu, Z., Li, G., Zong, X., Lei, Z., Wei, Y., Ma, J., Yang, X., Feng, X., 2021.
16 Multi-site infant brain segmentation algorithms: The iSeg-2019 Challenge. IEEE
17 Transactions on Medical Imaging.
- 18 Wang, F., Lian, C., Wu, Z., Zhang, H., Li, T., Meng, Y., Wang, L., Lin, W., Shen, D., Li, G.,
19 2019a. Developmental topography of cortical thickness during infancy. Proceedings of the
20 National Academy of Sciences 116, 15855-15860.
- 21 Wang, H., Suh, J.W., Das, S.R., Pluta, J.B., Craige, C., Yushkevich, P.A., 2012a. Multi-atlas
22 segmentation with joint label fusion. IEEE transactions on pattern analysis and machine
23 intelligence 35, 611-623.
- 24 Wang, L., Gao, Y., Shi, F., Li, G., Gilmore, J.H., Lin, W., Shen, D., 2015. LINKS:
25 Learning-based multi-source IntegratioN frameworK for Segmentation of infant brain
26 images. NeuroImage 108, 160-172.
- 27 Wang, L., Li, G., Adeli, E., Liu, M., Wu, Z., Meng, Y., Lin, W., Shen, D., 2018a. Anatomy -
28 guided joint tissue segmentation and topological correction for 6 - month infant brain MRI
29 with risk of autism. Human brain mapping 39, 2609-2623.
- 30 Wang, L., Li, G., Shi, F., Cao, X., Lian, C., Nie, D., Liu, M., Zhang, H., Li, G., Wu, Z., 2018b.
31 Volume-based analysis of 6-month-old infant brain MRI for autism biomarker identification

and early diagnosis, International Conference on Medical Image Computing and
Computer-Assisted Intervention. Springer, pp. 411-419.

Wang, L., Nie, D., Li, G., Puybureau, É., Dolz, J., Zhang, Q., Wang, F., Xia, J., Wu, Z., Chen,
J.-W., 2019b. Benchmark on automatic six-month-old infant brain segmentation algorithms:
The iSeg-2017 challenge. *IEEE transactions on medical imaging* 38, 2219-2230.

Wang, L., Shi, F., Gao, Y., Li, G., Gilmore, J.H., Lin, W., Shen, D., 2014. Integration of sparse
multi-modality representation and anatomical constraint for isointense infant brain MR
image segmentation. *NeuroImage* 89, 152-164.

Wang, L., Shi, F., Yap, P.-T., Gilmore, J.H., Lin, W., Shen, D., 2012b. 4D multi-modality tissue
segmentation of serial infant images. *PloS one* 7, e44596.

Wang, Z., Zou, N., Shen, D., Ji, S., 2020. Non-Local U-Nets for Biomedical Image
Segmentation, *AAAI*, pp. 6315-6322.

Wen, X., Zhang, H., Li, G., Liu, M., Yin, W., Lin, W., Zhang, J., Shen, D., 2019. First-year
development of modules and hubs in infant brain functional networks. *Neuroimage* 185,
222-235.

Wu, G., Wang, Q., Zhang, D., Nie, F., Huang, H., Shen, D., 2014. A generative probability
model of joint label fusion for multi-atlas based brain segmentation. *Medical image analysis*
18, 881-890.

Xu, Y., Cao, M., Liao, X., Xia, M., Wang, X., Jeon, T., Ouyang, M., Chalak, L., Rollins, N.,
Huang, H., 2019. Development and emergence of individual variability in the functional
connectivity architecture of the preterm human brain. *Cerebral Cortex* 29, 4208-4222.

Yushkevich, P.A., Piven, J., Hazlett, H.C., Smith, R.G., Ho, S., Gee, J.C., Gerig, G., 2006.
User-guided 3D active contour segmentation of anatomical structures: significantly
improved efficiency and reliability. *Neuroimage* 31, 1116-1128.

Zeng, G., Zheng, G., 2018. Multi-stream 3D FCN with multi-scale deep supervision for
multi-modality isointense infant brain MR image segmentation, 2018 IEEE 15th
International Symposium on Biomedical Imaging (ISBI 2018). IEEE, pp. 136-140.

Zhang, W., Li, R., Deng, H., Wang, L., Lin, W., Ji, S., Shen, D., 2015. Deep convolutional
neural networks for multi-modality isointense infant brain image segmentation. *NeuroImage*
108, 214-224.

- 1 Zhao, T., Xu, Y., He, Y., 2019. Graph theoretical modeling of baby brain networks. *NeuroImage*
- 2 185, 711-727.

3